# Efficient photocatalytic degradation of cationic and anionic dyes under visible light irradiation using TiO<sub>2</sub>\ZrO<sub>2</sub> nanocomposite

M. Kiruthigadevi <sup>a,\*</sup>, R. Mathammal <sup>a</sup>, P. Kumar <sup>b</sup>, S. Senapati <sup>b</sup>

<sup>a</sup> PG & Research Department of Physics, Sri Sarada College for Women
(Autonomous), Salem – 636 016, Tamilnadu

<sup>b</sup> Pravoga Institute of Education Research, Bangalore – 560085

 $TiO_2/ZrO_2$  nanocomposite are synthesized by hydrothermal method in two different molar ratios (60% $TiO_2/40\%ZrO_2$  & 40% $TiO_2/60\%ZrO_2$ ) to investigate their photocatalytic degradation. The synthesized composite was characterized using XRD, FT-IR, UV-Visible – DRS, HR – SEM and EDX analysis. The photocatalytic activity is assessed through the degradation of Rhodamine B (RhB) & Eosin Yellow (EY) dyes with three different dosages (5 mg, 10mg, 15mg) and exhibit 96% - 99% of degradation efficiency at 120 min. The photocatalytic studies reveals that both the composition exhibits better degradation efficiency compared to pure phase for both the dyes under visible light irradiation. Overall, the  $TiO_2/ZrO_2$  composite has exhibited superior photocatalytic efficiency for both cationic and anionic dyes.

(Received July 9, 2025, Accepted October 10, 2025)

Keywords: TiO<sub>2</sub> – ZrO<sub>2</sub> composite, Hydrothermal method, UV-Vis – DRS, HR SEM & EDX, Photodegradation

#### 1. Introduction

Photocatalysis is emerging as highly promising field in recent years due to its advanced oxidation process and has a considerable interest in its various uses in environmental remediation, particularly in breaking down persistent organic contaminants and mineralizing such harmful products into harmless byproducts under ambient conditions [1]. Among the various environmental concerns, the textile industry's explosive growth is a major factor in the buildup of refractory organic pollutants in synthetic dye effluents being among the most recalcitrant and hazardous pollutants in aquatic ecosystems [2]. These synthetic dyes exhibit high chemical stability, complex aromatic structures and low biodegradability making their removal through conventional wastewater treatment methods highly challenging. The release of these contaminants not only deteriorates the water quality but also disrupts aquatic ecosystem by reducing light penetration, inhibiting photosynthetic activity and also introducing toxic effects on aquatic flora and fauna [3-4]. Additionally, the long-term persistence of these pollutants leads to bioaccumulation and trophic transfer, causes severe risks to human health through exposure to mutagenic and carcinogenic intermediates. The conventional treatment techniques including coagulation, flocculation, adsorption, exhibit limitations in achieving the complete mineralization of these pollutants, there by necessitating the advancement of innovative and sustainable approaches [5]. By producing extremely reactive radical species when exposed to light, semiconductor-based catalysts are essential for the degradation of organic pollutants and artificial dyes, which facilitates the complete breakdown of complex contaminants into environmentally benign end products as CO2 and H2O [6 - 8]. So, researchers focus on developing a novel nanostructured photocatalysts, doped semiconductor and hybrid composite material further expands the scope of photocatalytic applications which is a viable technology for mitigating industrial pollution. Titanium dioxide (TiO<sub>2</sub>) and Zirconium dioxide (ZrO<sub>2</sub>) possess exceptional physicochemical properties, positioning them as crucial materials in various scientific and industrial applications. TiO<sub>2</sub> is renowned for its remarkable photocatalytic activity, high refractive index and strong oxidative potential but it restricts

<sup>\*</sup> Corresponding author: kiruthigamurugadas07@gmail.com https://doi.org/10.15251/DJNB.2025.204.1247

the absorption to UV region due to their band gap, necessitating structural modification or compositional tuning to extend its functionality into the visible spectrum [9 – 12]. Conversely,  $ZrO_2$  is characterized by its high thermal stability, excellent mechanical strength and chemical inertness. Despite these advantages,  $ZrO_2$  hinder its application in photocatalytic activity because of wide band gap, low charge carrier mobility, lack of redox activity and low surface adsorption [13 – 16]. Even though,  $TiO_2$  and  $ZrO_2$  have their unique strengths, both require further modifications to optimize their performance in photocatalytic and other advanced applications. Using the solution combustion approach, the synthesis of  $ZrO_2$ ,  $TiO_2$ , and  $ZrO_2$ - $TiO_2$  mixed oxides has been investigated by Polisetti et al. At an initial dye concentration of 25 ppm, they demonstrated enhanced photocatalytic performance in the degradation of four anionic dyes in two hours. Furthermore, the catalytic activity was assessed when  $H_2O_2$  salt (3 to 150 mM) was present. [17]. Kumari P et al. synthesized  $TiO_2$ ,  $ZrO_2$  and  $TiO_2 - ZrO_2$  mixed oxides through the sol-gel technique, and their photocatalytic activity was evaluated by measuring the degradation of eosin dye under UV light, showed a degradation efficiency of 87.87 % within 5 hours for  $TiO_2 - ZrO_2$  composite, with particle size of about 41 nm [18].

In order to increase photocatalytic activity, oxalic acid dihydrate was employed at different ratios as a reducing agent during the hydrothermal synthesis of a TiO<sub>2</sub>/ZrO<sub>2</sub> composite. The final composite was examined to assess its optical, morphological, and structural characteristics as well as its advantageous band gap for efficient degradation of eosin yellow dye and Rhodamine B (RhB) when exposed to visible light. Additionally, the TiO<sub>2</sub>/ZrO<sub>2</sub> composite's biological activity was carefully evaluated to ascertain its toxicity to aquatic life and other environmental factors, guaranteeing its potential for safe use in environmental restoration.

# 2. Characterization techniques

In order to determine the crystalline phases and crystalline size, which are also, determined using the Scherrer equation, the diffraction patterns are produced utilising a Cu Kα ((1.5406Å) radiation-equipped X-ray diffractometer (Malvern PANalytical, Empyrean, Netherlands) in a 2θ range of  $20^{\circ} - 80^{\circ}$ . To assess the functional groups and chemical bonding interactions, the Perkin Elmer spectrometer records the FTIR spectrum, which spans from 4000 cm-1 to 400 cm<sup>-1</sup>. Using the Shimadzu UV 2600i, the UV-DRS reflectance spectra are acquired in order to examine the band gap energy using Tauc's graphic analysis. The FEI-QUANTA FEG 200F is used to perform SEM pictures and EDX spectrums with a resolution of 1.2 nm in order to ascertain the elemental composition, particle size distribution, and surface morphology. A PHI-VERSAPROBE III spectroscopy (monochromatic X-ray beam of 15µm) is employed in X-ray Photoelectron Spectroscopy (XPS), which ascertains the oxidation states and surface composition of the elements to provide information on the electronic structure and chemical interactions of the nanocomposites. The photocatalytic activity of the TiO<sub>2</sub>/ZrO<sub>2</sub> nanocomposite is evaluated at regular intervals in Prayoga Institute of Education Research under visible light irradiation by measuring the absorbance of the dye solution (Rhodamine B (RhB) & Eosin yellow (Eosin Y)) at a characteristic wavelength using a UV-Vis spectrophotometer.

#### 3. Materials and Methods

#### 3.1. Samples preparation

The  $TiO_2/ZrO_2$  nanocomposite are synthesized via the hydrothermal method using commercially available analytical grade reagents.

$$C_2H_2O_4.2H_2O \rightleftharpoons C_2O_4^{2-} + 2H^+$$
 (1)

$$TiO_2 + C_2O_4^{2-} \rightarrow [Ti(C_2O_4)]^{2-}$$
 (2)

$$ZrO_2 + C_2O_4^{2-} \rightarrow [Zr(C_2O_4)]^{2-}$$
 (3)

Titanium dioxide (TiO<sub>2</sub>) and Zirconium dioxide (ZrO<sub>2</sub>) are employed in two different molar ratios to obtain distinct composite formulations. To improve the dispersion and interaction of the metal oxides in Equation (1), oxalic acid dehydrates (C<sub>2</sub>H<sub>2</sub>O<sub>4</sub>.2H<sub>2</sub>O) is used as a chelating and stabilizing agent. Oxalic acid dihydrate is dissolved in 100 millilitres of distilled water and agitated constantly to create a 2M solution. The TiO<sub>2</sub> and ZrO<sub>2</sub> are introduced into the oxalic acid solution (equation 2 & 3) in a predetermined ratios TiO<sub>2</sub> (60 wt%):ZrO<sub>2</sub> (40 wt%) and TiO<sub>2</sub> (40 wt%):ZrO<sub>2</sub> (60 wt%) and stirred vigorously for 5hours to ensure homogeneous mixing followed by adding isopropyl alcohol as a surfactant to improve dispersion.

$$[Ti(C_2O_4)]^{2-} + 2H_2O \rightarrow Ti(OH)_4 + (C_2O_4)^{2-}$$
 (4)

$$[Zr(C_2O_4)]^{2-} + 2H_2O \rightarrow Zr(OH)_4 + (C_2O_4)^{2-}$$
 (5)

To aid in crystallisation, the resultant mixture is placed in an autoclave lined with Teflon and heated to 150°C for 12 hours and nanocomposite formation. While heating in hydrothermal reactor, the oxalate complex metal ions form a metal hydroxide intermediates due to hydrolysis and condensation which shows in Equation (4 & 5).

$$Ti(OH)_4 + Zr(OH)_4 \rightarrow TiO_2/ZrO_2 + 2H_2O(6)$$

These metal hydroxides undergo polycondensation leading to formation of composite. The synthesized materials are washed ethanol and deionised water several times to eliminate contaminants, and then dried at 100 °C to eliminate moisture. To create a consistent particle size, the dried material is finely ground with a mortar and pestle. The grinned material undergo calcination at 700 °C for 6 hours to enhance crystallinity and phase stability.

# 3.2. Photocatalytic dye-degradation

Using slightly modified versions of previously published techniques, the effectiveness of the synthesised nanoparticles in photocatalytically degrading rhodamine B (RB) and eosin yellow (EY) dye in a visible lamp source was assessed and contrasted with four distinct samples at room temperature [19]. To create a homogenous dye solution, a 10 ppm solution of rhodamine B and eosin yellow were made in 50 mL of Type 1 ultrapure water (Merck Millipore, India) and swirled on a magnetic stirrer. A Heber Scientific yearly photoreactor was used to conduct the photocatalytic investigation (HIPR -MP250) under visible with 240 W halogen lamp as light source, it emits photons with wavelength of 300-790 nm. The degradation study was done for a period of 120 mins and solution was analysed at regular interval of 15 mins. To evaluate and maximise the impact of nanoparticle concentrations on the degradation process, different concentrations of nanoparticles were introduced to the dye solutions. The reaction mixture was stirred in the dark for half an hour in order to reach equilibrium. After then, the reaction mixture was exposed to radiation for ninety minutes [20]. Two millilitres of the reaction mixture were taken every fifteen minutes, and the absorbance readings at 545 nm were recorded using the Evolution one UV-Vis spectrophotometer (Thermo Fisher Scientific, India). The photocatalytic degradation efficiency of the nanoparticles was calculated using the formula:

Degradation efficiency (%) = 
$$(A_0 - A_t)/A_0 \times 100$$

where A<sub>t</sub> is the absorbance at a specific time, and A0 is the dye's absorbance at the start.

The rate constants for photocatalytic degradation were studied using the degradation fit pseudo-first-order reaction model, which is written as: [21, 22 & 23]

$$ln(C_0/C) = kt$$

where  $C_0$  is the dye's initial concentration, C is the dye concentration at time t, and k is the dye degradation rate constant.

#### 4. Result and discussion

#### 4.1. XRD analysis

Powder X-ray diffraction has been used to determine the crystal structure and phase modification of  $TiO_2$  and  $ZrO_2$ , and Figure 1 displays the diffraction pattern. The diffraction pattern exhibits intense peak at  $2\theta = 25.75^{\circ}$  indexing to (101) plane of tetragonal structure of  $TiO_2$ . The peaks at  $2\theta = 25.75^{\circ}$ ,  $38.24^{\circ}$ ,  $48.47^{\circ}$ ,  $69.19^{\circ}$ ,  $75.45^{\circ}$  corresponds to (101), (004), (200), (116), (215) reflections, respectively, have been observed and are consistent with the characteristic peaks of anatase phase (JCPDS card No. #894203) whereas the reflections at plane (110), (103), (211), (002) are observed at  $2\theta = 27.08^{\circ}$ ,  $36.52^{\circ}$ ,  $55.49^{\circ}$ ,  $63.11^{\circ}$  which is attributed to rutile phase (JCPDS card No. 21 - 1276), indicating the coexistence of both anatase and rutile phases. The XRD pattern of  $TiO_2$  reveals that the anatase phase ( $\sim$ 54.51%) is dominant contributor than rutile phase ( $\sim$ 45.49%) and the proportion of both phases has been determined using a Spurr Equation (7 & 8).

% Anatase = 
$$\frac{I_A}{(I_A + (0.79 \times I_R))} \times 100$$
 (7)

% Rutile = 
$$100 - \%$$
 Anatase (8)

whereas  $I_A$  – intensity of anatase at (101) plane and  $I_R$  – intensity of rutile at (110) plane. For ZrO<sub>2</sub> the more intense peak is observed at  $2\theta = 30.52^{\circ}$  with characteristic crystal plane at (101). The peaks appeared at  $2\theta = 30.52^{\circ}$ ,  $35.27^{\circ}$ ,  $50.66^{\circ}$ ,  $60.20^{\circ}$ ,  $63.07^{\circ}$ ,  $74.84^{\circ}$  these correlates to the tetragonal structure of ZrO<sub>2</sub>'s (101), (110), (020), (121), (202), and (220) reflections (JCPDS card No. 80 – 0965). The calcination process at 700°C facilitated a phase transition in ZrO<sub>2</sub>, yielding a transformation from the monoclinic to tetragonal phase accompanied by an enhancement in crystallinity. The XRD patterns of mixed oxide of TiO<sub>2</sub> - ZrO<sub>2</sub> (60 and 40 mol %) exhibit a combination of characteristic peaks corresponding to both phases, indicating the successful formation of a mixed - phase structure. The intensity and presence of the peak in mixed phase of TiO<sub>2</sub>/ZrO<sub>2</sub> are influenced by the compositional ratio of two phase. As TiO<sub>2</sub> (60%) increases, accompanied by a corresponding decrease in ZrO<sub>2</sub> (40%), the peaks of TiO<sub>2</sub> gain dominance in intensity and presence of peaks with respective plane surpassing those of ZrO<sub>2</sub>. Conversely, when ZrO<sub>2</sub> (60%) is the predominant component, its peaks exhibit enhanced intensity and prominence overshadowing those of TiO<sub>2</sub> (40%). The high intensity peaks in the spectra show how crystallinity is high in the samples. Subsidiary peaks in the TiO<sub>2</sub>/ZrO<sub>2</sub> nanocomposite's XRD spectrum suggest a heterogeneous nanostructure, possibly the result of core-shell structure development, which can affect the material's characteristics and behavior [24 – 25]. The Debye Scherrer Equation is used to determine the average crystalline size (9),

$$D = \frac{k\lambda}{\beta \cos \theta} nm \tag{9}$$

In this case, D stands for average crystalline size, k for dimensionless form factor,  $\lambda$  for X-ray wavelength,  $\beta$  for full width at half strength (FWHM), and  $\theta$  for Bragg's diffraction angle. For ZrO<sub>2</sub>, TiO<sub>2</sub>, and TiO<sub>2</sub>-ZrO<sub>2</sub> nanocomposite, the average crystalline size showed a consistent crystallite size of 14 nm.

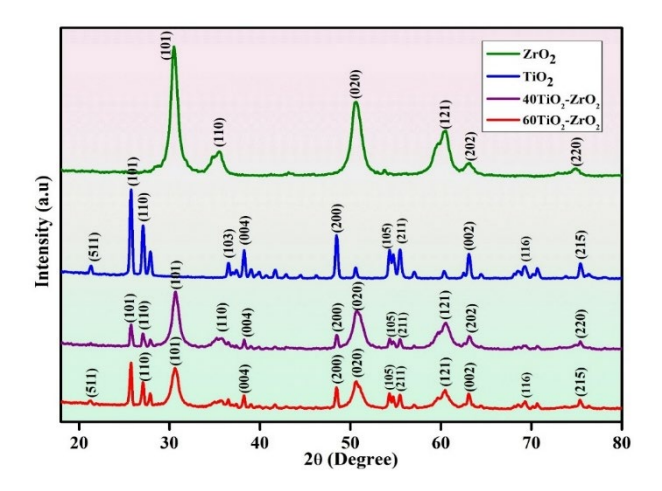


Fig. 1. XRD pattern of  $ZrO_2$ ,  $TiO_2$  and  $TiO_2 - ZrO_2$  nanocomposite.

## 4.2. FT – IR analysis

Utilizing Fourier Transform Infrared (FT-IR) spectroscopy, the vibrational characteristics of ZrO<sub>2</sub>, TiO<sub>2</sub>, and TiO<sub>2</sub>-ZrO<sub>2</sub> nanocomposite are examined. The FTIR spectrum is presented in Figure 2, spanned a wavenumber range of 4000 – 500 cm<sup>-1</sup> which reveals distinct vibrational modes corresponding to the molecular structure, bonding configuration of individual oxides and their composite counterpart subsequent to hydrothermal and calcination treatment. A large peak at 471–798 cm<sup>-1</sup> in the TiO<sub>2</sub> FTIR spectrum is ascribed to Ti–O stretching vibrations, which are a feature of the anatase phase of TiO<sub>2</sub>. The peak's broad nature is caused by the distribution of Ti–O–Ti bond lengths and angles. The Ti-O stretching vibration is also responsible for the sharp peak at 1081 cm<sup>-1</sup>, whereas the O-H bending vibration is responsible for the low concentration of surface hydroxyl groups at 1627 cm<sup>-1</sup>. There is a large broad peak in the ZrO<sub>2</sub> spectrum between 477 and 782 cm<sup>-1</sup>, which indicates a greater distribution of Zr–O stretching vibrations. Zr–O stretching vibrations are also responsible for the peak at 1086 cm<sup>-1</sup>. The O-H stretching vibration is responsible for the broad peaks visible at 3432 cm<sup>-1</sup> for TiO<sub>2</sub> and 3427 cm<sup>-1</sup> for ZrO<sub>2</sub>. Therefore, the metal-oxygen stretching modes of ZrO<sub>2</sub> and TiO<sub>2</sub> are confirmed by the FT-IR spectra, and they are in perfect agreement with previously published data [26 – 27].

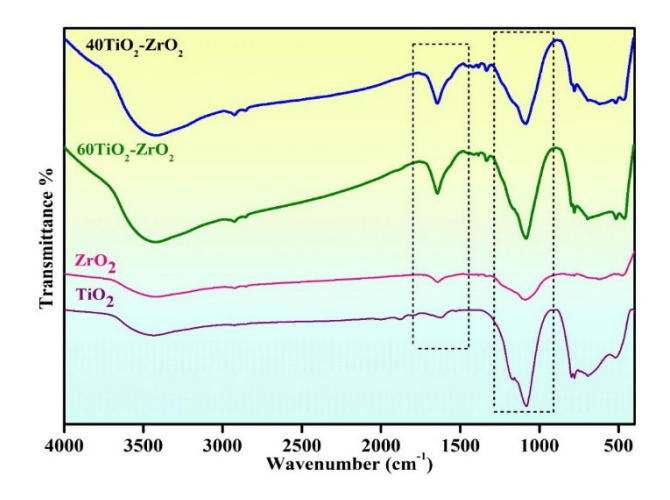


Fig. 2. FT - IR spectrum of  $TiO_2$ ,  $ZrO_2$ ,  $TiO_2/ZrO_2$  nanocomposites.

## 4.3. Optical diffuse reflectance spectroscopy (DRS) analysis

The Kubelka-Munk function, which establishes a link between the reflectance data and optical properties of the materials using the corresponding Equation (10), is computed using the diffuse reflectance spectra acquired from the samples. Figure displays the reflectance spectra of both pure and composite materials, which were obtained at room temperature between 200 and 1400 nm.

$$F(R) = \frac{1 - R^2}{2R} \tag{10}$$

where F(R) is the Kubelka-Munk function and R is reflectance. The optical energy gap is determined using the tauc's relation Equation (11) that is derived from the Kubelka-Munk function.

$$F(R) h\nu = A (h\nu - E_q)^2$$
(11)

Figure (3) displays the UV DRS spectra of the oxides. The results show that pure TiO<sub>2</sub> has a band gap of 3.34 eV (anatase), while ZrO<sub>2</sub> has a larger optical band gap of 3.88 eV. The band gap values in the mixed phase TiO<sub>2</sub>/ZrO<sub>2</sub> composites were affected by the composition. 40% TiO<sub>2</sub>/ZrO<sub>2</sub> exhibits a little larger bandgap of 3.33 eV while 60% TiO<sub>2</sub>/ZrO<sub>2</sub> exhibits a band gap of 3.32 eV, both of which are consistent with previously published results [28–29]. The creation of interfacial states that affect the likelihood of electron transitions is the cause of these minor variations in the bandgap energy for the mixed phase composites. When Zr4+ ions are added to the TiO<sub>2</sub> lattice, the ionic radius mismatch causes structural distortions that can produce localised defect states and change the density of states at the conduction and valence bands [30–31]. Furthermore, ZrO<sub>2</sub> acts as an electron trapping site to limit rapid charge recombination and stabilise the TiO<sub>2</sub> phase, improving photocatalytic effectiveness.

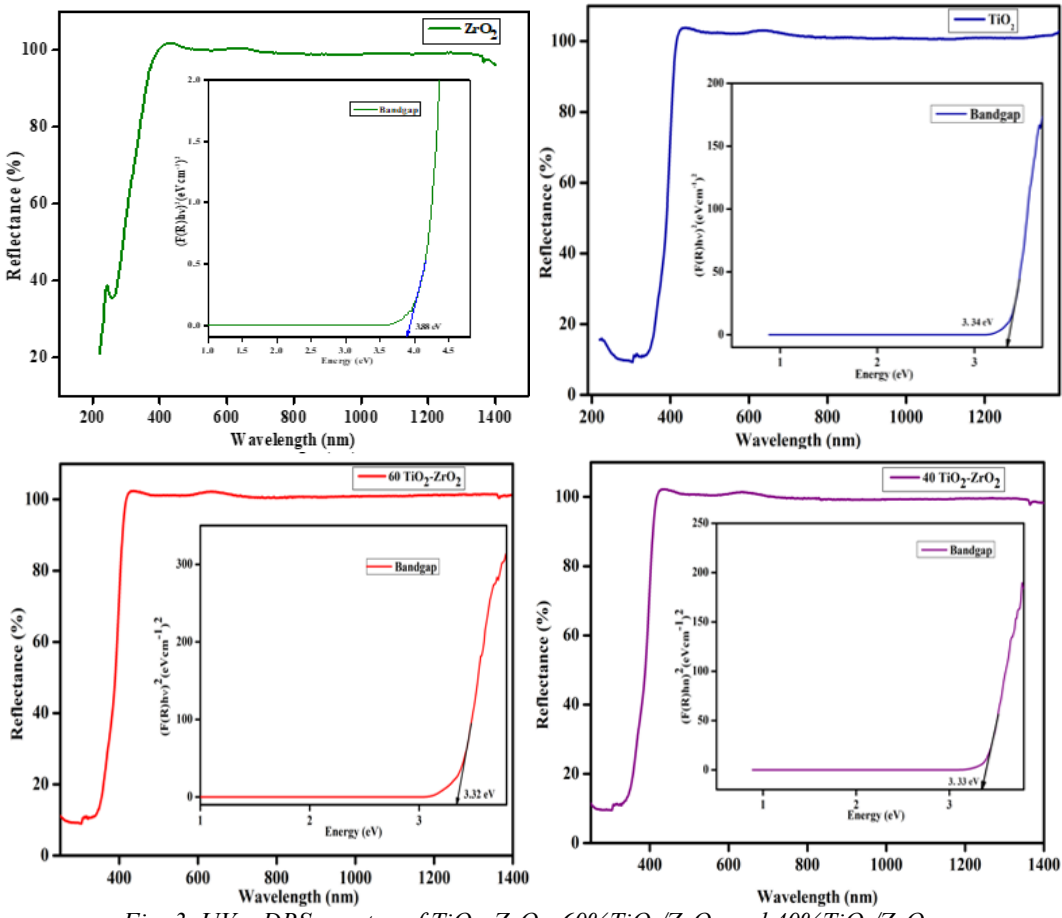


Fig. 3. UV – DRS spectra of TiO<sub>2</sub>, ZrO<sub>2</sub>, 60%TiO<sub>2</sub>/ZrO<sub>2</sub> and 40%TiO<sub>2</sub>/ZrO<sub>2</sub>.

Therefore, the synergistic interaction between Ti<sup>4+</sup> and Zr<sup>4+</sup> ions, which influences the dynamics of charge carriers, can also be ascribed to the shift in bandgap [32–33]. Effective charge separation is made possible by the creation of heterojunctions at the TiO<sub>2</sub>/ZrO<sub>2</sub> interface, which enhances optoelectronic characteristics and opens up possibilities for use in energy conversion, photovoltaics, photocatalysis, thermoelectric, and environmental remediation technologies [34–35].

# 4.4. HR – SEM and EDX analysis

HR-SEM & EDX are used to evaluate the surface morphology, particle size, and existing elements. The SEM images of pure TiO<sub>2</sub> nanoparticles is shown in Figure 4(a & b), which shows the cluster development of a non-uniform flattened semi-globular structure. Pure TiO<sub>2</sub> nanoparticles have an average size of 71.9 nm and range in size from 37.7 nm to 82.5 nm. The irregular elongated oval structure of ZrO<sub>2</sub> is visible in the SEM pictures (Figure 4.c & d). The average particle size is 66.6 nm, with a range of 23.7 nm to 75.1 nm. Both the ZrO<sub>2</sub> and TiO<sub>2</sub> nanoparticles exhibit mild aggregation as a result of the 700°C calcination temperature. The composition of the materials is confirmed through impregnation of TiO<sub>2</sub> and ZrO<sub>2</sub>.

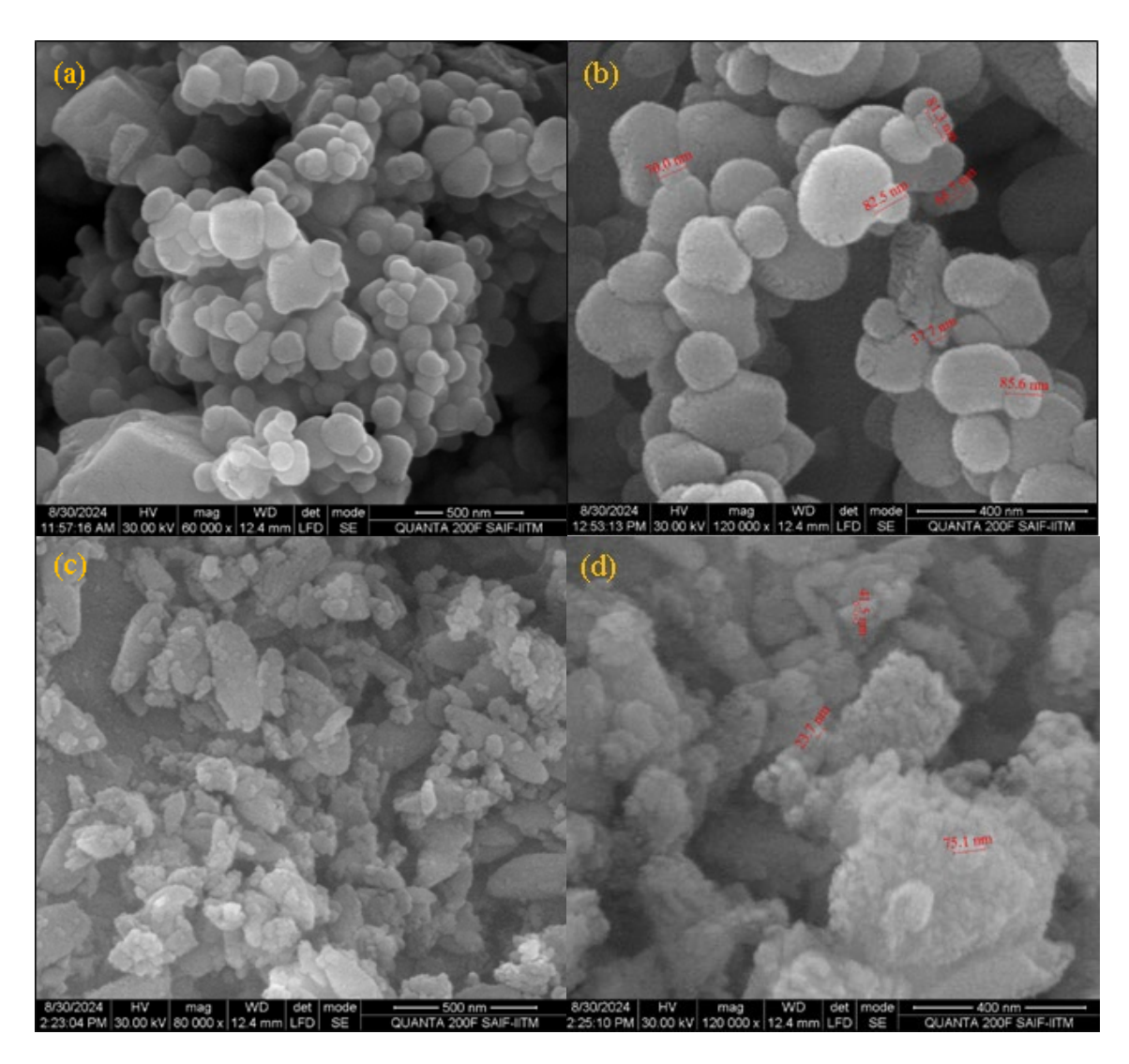


Fig. 4. SEM images of  $TiO_2(a \& b)$ ,  $ZrO_2(c \& d)$  at 700°C.

The composite consisting predominantly of TiO<sub>2</sub> with a minor proportion of ZrO<sub>2</sub> confirms the presence of 60%TiO<sub>2</sub>/ZrO<sub>2</sub> with an average particle size of 48.1 nm is presented in Figure 5. Conversely, a ZrO<sub>2</sub> impregnated with a minor inclusion of TiO<sub>2</sub> confirms the presence of 40%TiO<sub>2</sub>/ZrO<sub>2</sub> and the average particle size is 38.63 nmwhich is shown in Figure 6. Figure 7 shows the average particle size distribution for both pure and mixed materials. The EDX analysis reveals the distinct peaks corresponding to Titanium (Ti), Zirconium (Zr), Oxygen (O) at specific energy levels. In 60%TiO<sub>2</sub>/ZrO<sub>2</sub>, the Ti peaks exhibit higher intensity relative to Zr and O corresponding to 34.88 Wt% of Ti and 18.82 Wt% of Zr whereas in 40%TiO<sub>2</sub>/ZrO<sub>2</sub>, Zr peaks are more prominent than those Ti and O, corresponding to 20.21Wt% of Ti and 38.58 Wt% of Zr. The remaining weight% of both the sample composition is attributed to oxygen which is responsible for formation of radical during degradation process which is presented in Table 1 & 2. This observation aligns well with previously published literature [36].

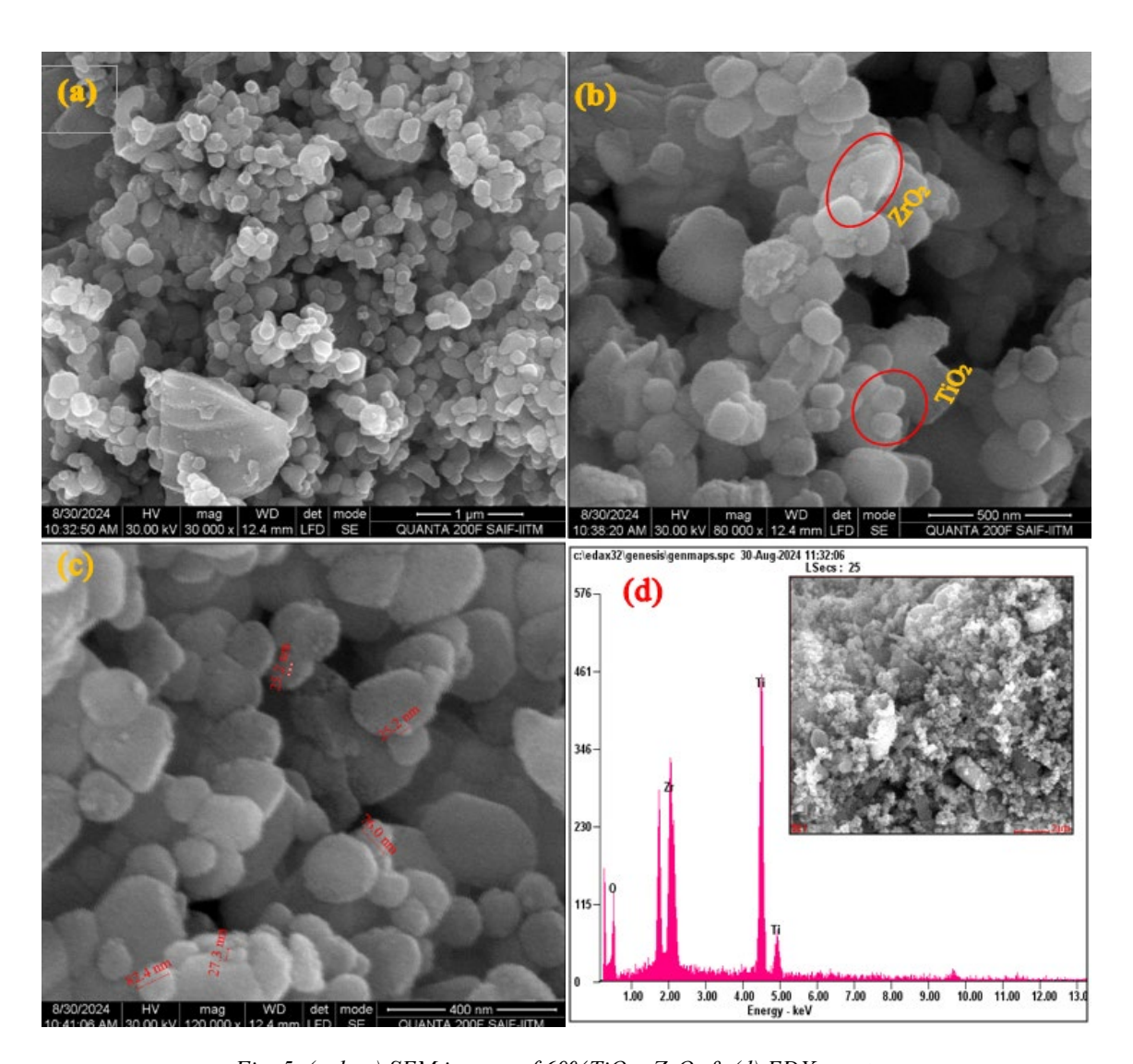


Fig. 5. (a, b, c) SEM images of 60%TiO<sub>2</sub> - ZrO<sub>2</sub> & (d) EDX spectra.

Table 1. Atomic % & Weight % from EDX spectrum of 60%TiO<sub>2</sub> - ZrO<sub>2</sub>.

Element	Wt%	At%
ОК	46.29	75.59
TiK	34.88	19.02
ZrK	18.82	05.39

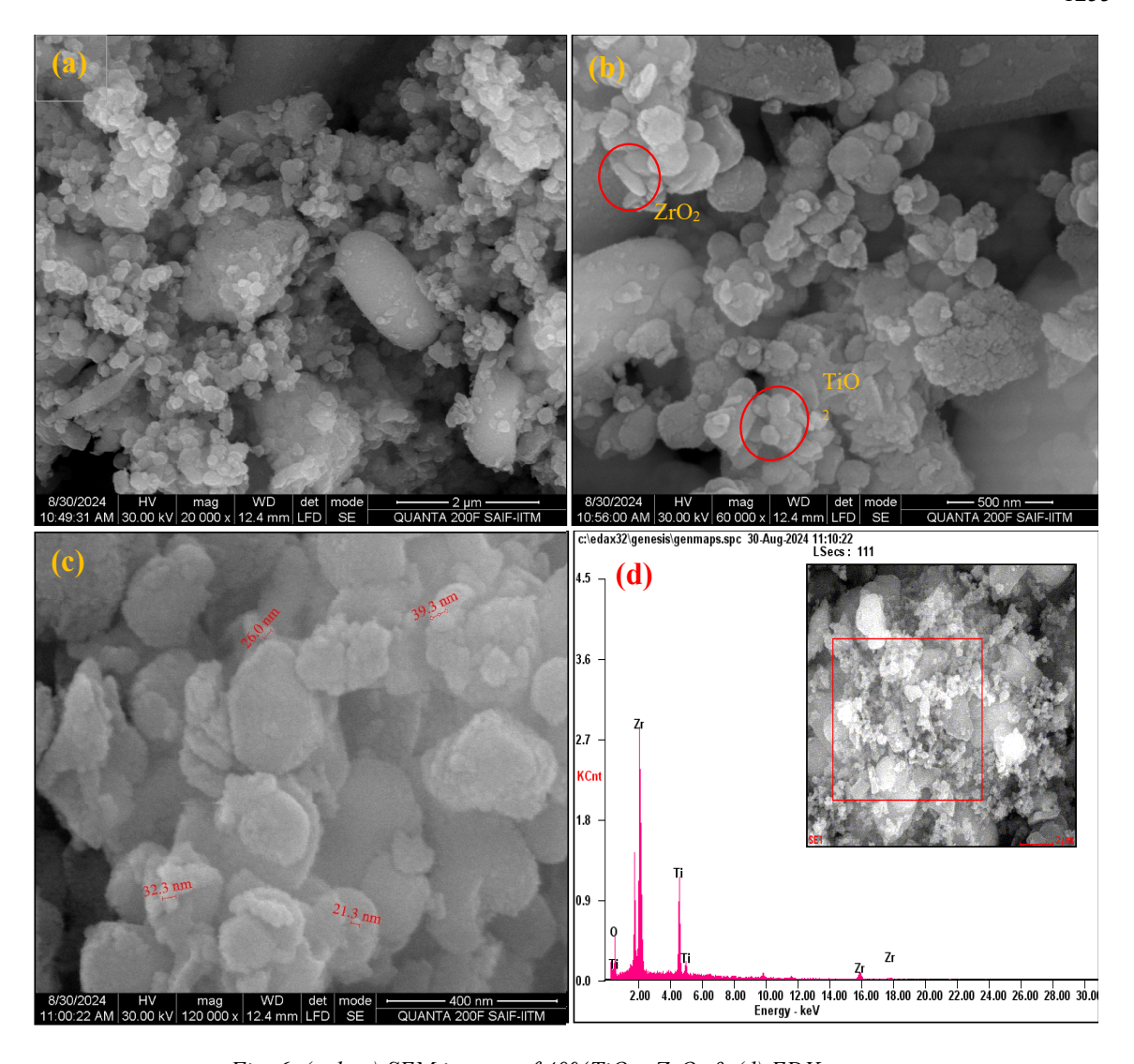


Fig. 6. (a, b, c) SEM images of 40%TiO<sub>2</sub> - ZrO<sub>2</sub> & (d) EDX spectra.

Table 2. Atomic % & Weight % from EDX spectrum of  $40\% TiO_2$  -  $ZrO_2$ .

Element	Wt%	At%
ОК	41.21	75.30
TiK	20.21	12.34
ZrK	38.58	12.36

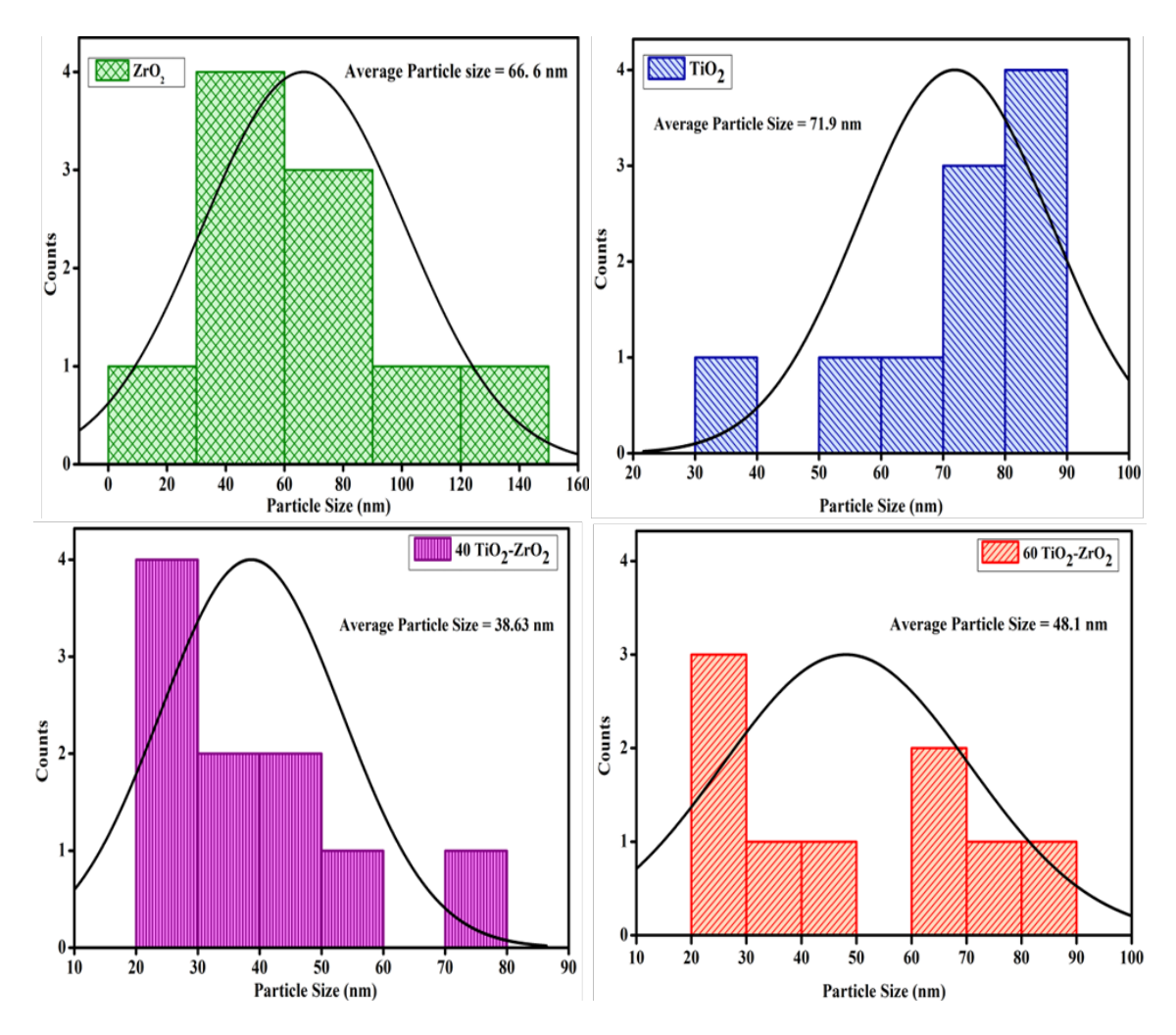


Fig. 7. Particle size distribution curves of TiO<sub>2</sub>, ZrO<sub>2</sub>, TiO<sub>2</sub>-ZrO<sub>2</sub>nanocomposites.

# 4.5. XPS analysis

One popular method for determining the elemental makeup of the as-prepared TiO<sub>2</sub>, ZrO<sub>2</sub>, utilising X-ray photoelectron spectroscopy (XPS), 60% TiO<sub>2</sub>/ZrO<sub>2</sub> and 40% TiO<sub>2</sub>/ZrO<sub>2</sub> nanoparticles are examined. The broad survey spectra of the nanomaterials TiO<sub>2</sub>, ZrO<sub>2</sub>, 60% TiO<sub>2</sub>/ZrO<sub>2</sub>, and 40% TiO<sub>2</sub>/ZrO<sub>2</sub> are displayed in Figure 8(a). The elements O, Ti, and Zr are present in both pure nanomaterials and different concentrations of nanocomposites, according to these survey spectra. High-resolution spectra were taken in order to better investigate the data related to the valence states, binding energies, and chemical bonds of the components contained in the 40%TiO<sub>2</sub>/ZrO<sub>2</sub> combination. The high-resolution XPS spectra for zirconium, titanium, and oxygen are shown in Figure 8(b-d), respectively. There were two deconvoluted peaks at 530.9 and 533.4 eV in the 40%TiO<sub>2</sub>/ZrO<sub>2</sub> O1s XPS spectra. The first high-intensity peak, which is associated with the binding energy of 530.7 eV, is the result of the interaction between zirconium and oxygen (Zr-O) and titanium and oxygen (Ti-O). The second, lower-intensity signal, which was detected at 532.5 eV, is caused by hydroxyl groups (OH) on the surface of the nanocomposite. Figure 8c shows the deconvolution of the high-resolution Ti 2 p spectrum into two distinctive peaks at 457.7 and 463.3 eV, respectively, which are attributed to the spin-orbit components of Ti  $(2p_{3/2})$  and Ti  $(2p_{1/2})$ . The detected binding energy peaks confirm the presence of Ti<sup>4+</sup> oxidation states and the successful formation of TiO<sub>2</sub> in the nanocomposite. The Zr 3d core-level spectrum (Figure 8d) of the 40%TiO<sub>2</sub>/ZrO<sub>2</sub> nanocomposite shows two deconvoluted peaks at 181.1 and 183.7 eV. These peaks are ascribed to the spin-orbit components of Zr (3d<sub>5/2</sub>) and Zr (3d<sub>3/2</sub>). The 40%TiO<sub>2</sub>/ZrO<sub>2</sub>

nanocomposite's  $Zr^{4+}$  oxidation state is confirmed by the observed peaks. Consequently, the XPS examination shows that the 40%  $TiO_2/ZrO_2$  nanocomposite as synthesised contains  $TiO_2$  and  $ZrO_2$  nanoparticles.

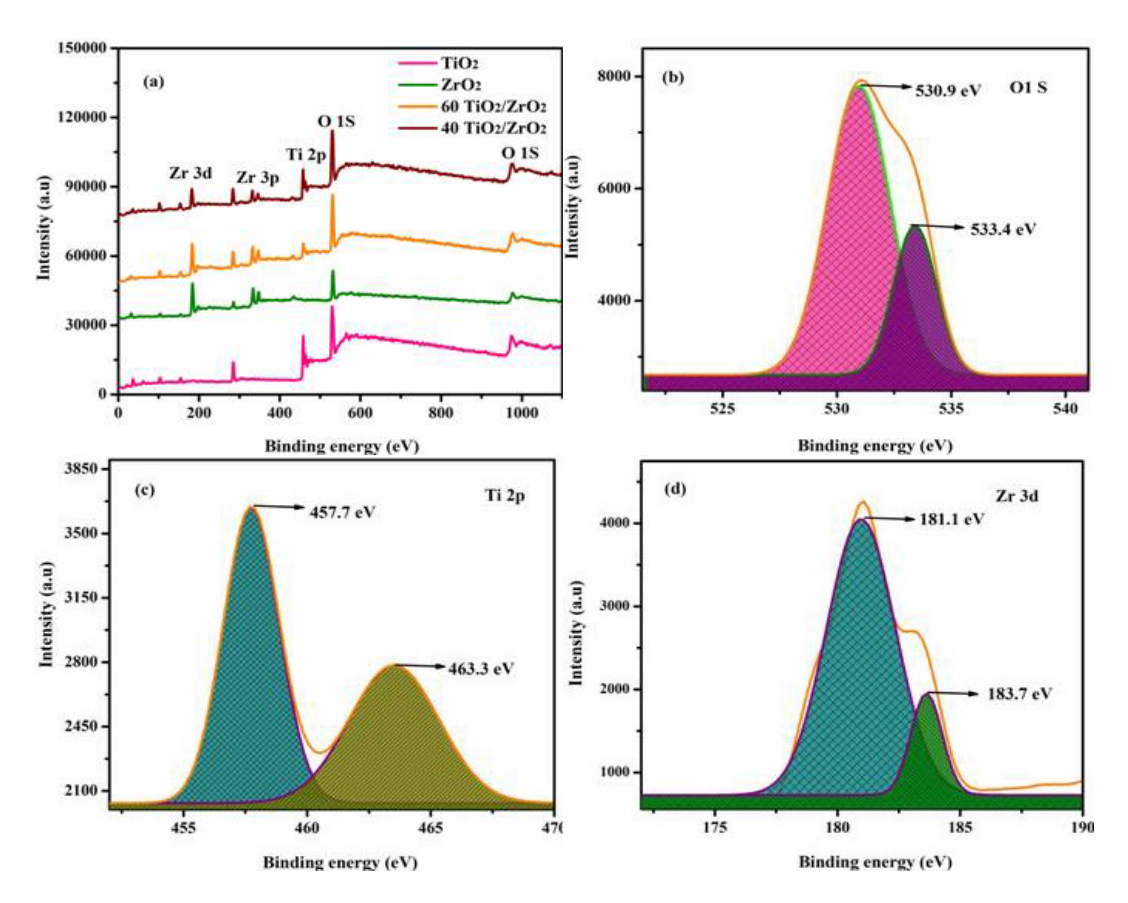


Fig. 8. a) XPS survey spectrum of TiO<sub>2</sub>, ZrO<sub>2</sub>, 60%TiO<sub>2</sub>/ZrO<sub>2</sub> and 40%TiO<sub>2</sub>/ZrO<sub>2</sub>. High-resolution deconvoluted XPS spectra of b) O1s, c) Ti 2p and Zr 3d of 40%TiO<sub>2</sub>/ZrO<sub>2</sub> concentration.

# 4.6. Dye degradation

Four distinct samples were used to examine the photocatalytic activity of the nanocomposites: pure TiO<sub>2</sub>, pure ZrO<sub>2</sub>, and a composite material with a 60% TiO<sub>2</sub>/ZrO<sub>2</sub> composition and 40% TiO<sub>2</sub>/ZrO<sub>2</sub> content. The percentage of rhodamine B and eosin yellow figures 9 and 10 shows the degradation of dyes when exposed to visible light. Eosin yellow and rhodamine B both have absorption maxima (λmax) of 510 and 545 nm, respectively. Absorption values at these wavelengths were measured as a function of irradiation time when a nanocomposite photocatalyst was present. Pure TiO<sub>2</sub> and ZrO<sub>2</sub> photocatalysts were used to compare the photocatalytic activity of TiO<sub>2</sub>/ZrO<sub>2</sub> composites. To determine the impact of photocatalyst concentration on the degradation efficiency, the dosage of the catalyst was varied between 5, 10, 15 mg and 5, 10 mg for degradation of RB and EY respectively. At all concentrations, the photocatalysts of 60%TiO<sub>2</sub> – ZrO<sub>2</sub>, 40%TiO<sub>2</sub>  $-\mathrm{ZrO}_2$  and pure  $\mathrm{TiO}_2$ , were able to degrade the dyes (Figure 9). Interestingly even at a lower dosage (5 mg), these photocatalysts facilitate the degradation of both the dyes RB and EY (10 ppm). The 60%TiO<sub>2</sub> – ZrO<sub>2</sub> was able to degrade both rhodamine B and eosin yellow, yet its activity was not as efficient as 40%TiO<sub>2</sub> – ZrO<sub>2</sub>. The 40%TiO<sub>2</sub> – ZrO<sub>2</sub> achieved the best photocatalytic activity among other because TiO<sub>2</sub> and ZrO<sub>2</sub>. Although pure TiO<sub>2</sub> showed similar degradation, its photocatalytic performance was slower than 40%TiO<sub>2</sub> – ZrO<sub>2</sub>. Similarly, pure ZrO<sub>2</sub> performed the poorest for the cationic dye RB, which could be due to its larger bandgap. The poor degradation efficiencies of pure TiO<sub>2</sub> and pure ZrO<sub>2</sub>, were low (Figure 9c and 9d) could be attributed to the narrower light absorption range and the increased electron-hole pair recombination rate [37, 38].

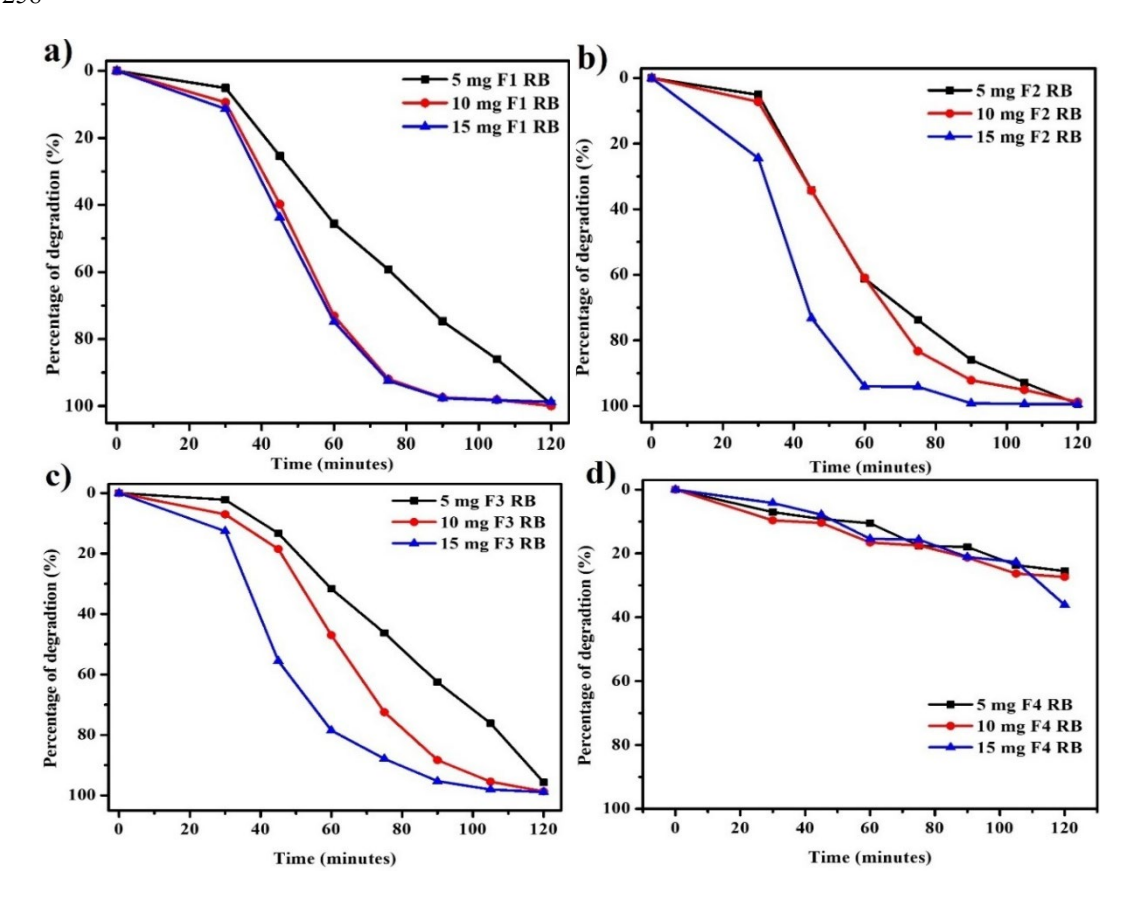


Fig. 9. Degradation percentage of rhodamine B over time with different concentrations of catalysts. a)  $F1 - 60\%TiO_2 - ZrO_2b$ ) F2  $40\%TiO_2 - ZrO_2$  c) F3 – pure  $TiO_2$  and d) F4 – pure  $ZrO_2$ .

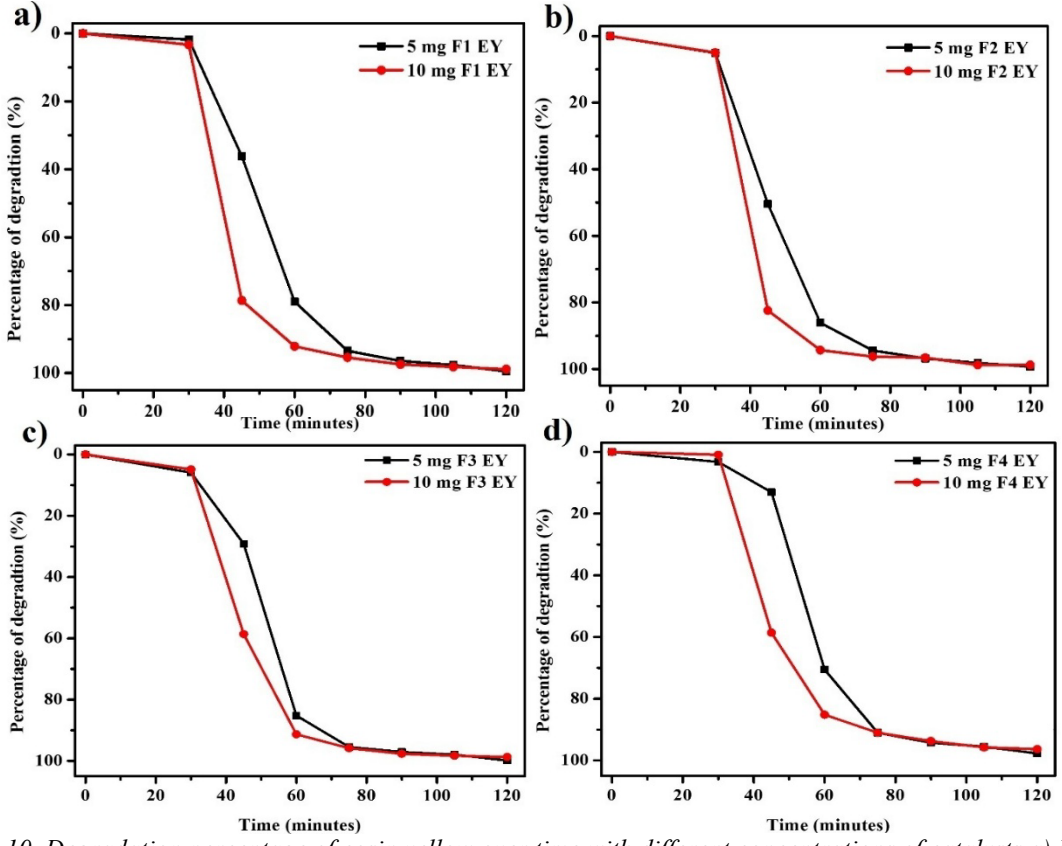


Fig. 10. Degradation percentage of eosin yellow over time with different concentrations of catalysts a)  $F1 - 60\%TiO_2 - ZrO_2$ , b)  $F2 + 40\%TiO_2 - ZrO_2$ , c)  $F3 - pure TiO_2$  and d)  $F4 - pure ZrO_2$ .

The degradation results of rhodamine B revealed that  $60\% \text{ TiO}_2 - \text{ZrO}_2$ ,  $40\% \text{TiO}_2 - \text{ZrO}_2$  and pure  $\text{TiO}_2$  samples at 5 mg dosage have shown a gradual trend in degradation whereas the 10 mg and 15 mg dosages showed a rapid trend with respect to time. The extent of dye degradation achieved is 96-99% for samples  $60\% \text{ TiO}_2 - \text{ZrO}_2$ ,  $40\% \text{TiO}_2 - \text{ZrO}_2$  and pure  $\text{TiO}_2$  at all the dosages. Sample pure  $\text{ZrO}_2$  at 15 mg dosage showed only 36% degradation over the same time period signifying that the composites of  $\text{TiO}_2$  and  $\text{ZrO}_2$  has a better efficiency than pure phase of the material. Although pure  $\text{TiO}_2$  has shown 98% degradation, the time taken for degradation at each interval is more than  $60\% \text{ TiO}_2 - \text{ZrO}_2$  and  $40\% \text{TiO}_2 - \text{ZrO}_2$ . Overall  $40\% \text{TiO}_2 - \text{ZrO}_2$  showed a better degradation efficiency.

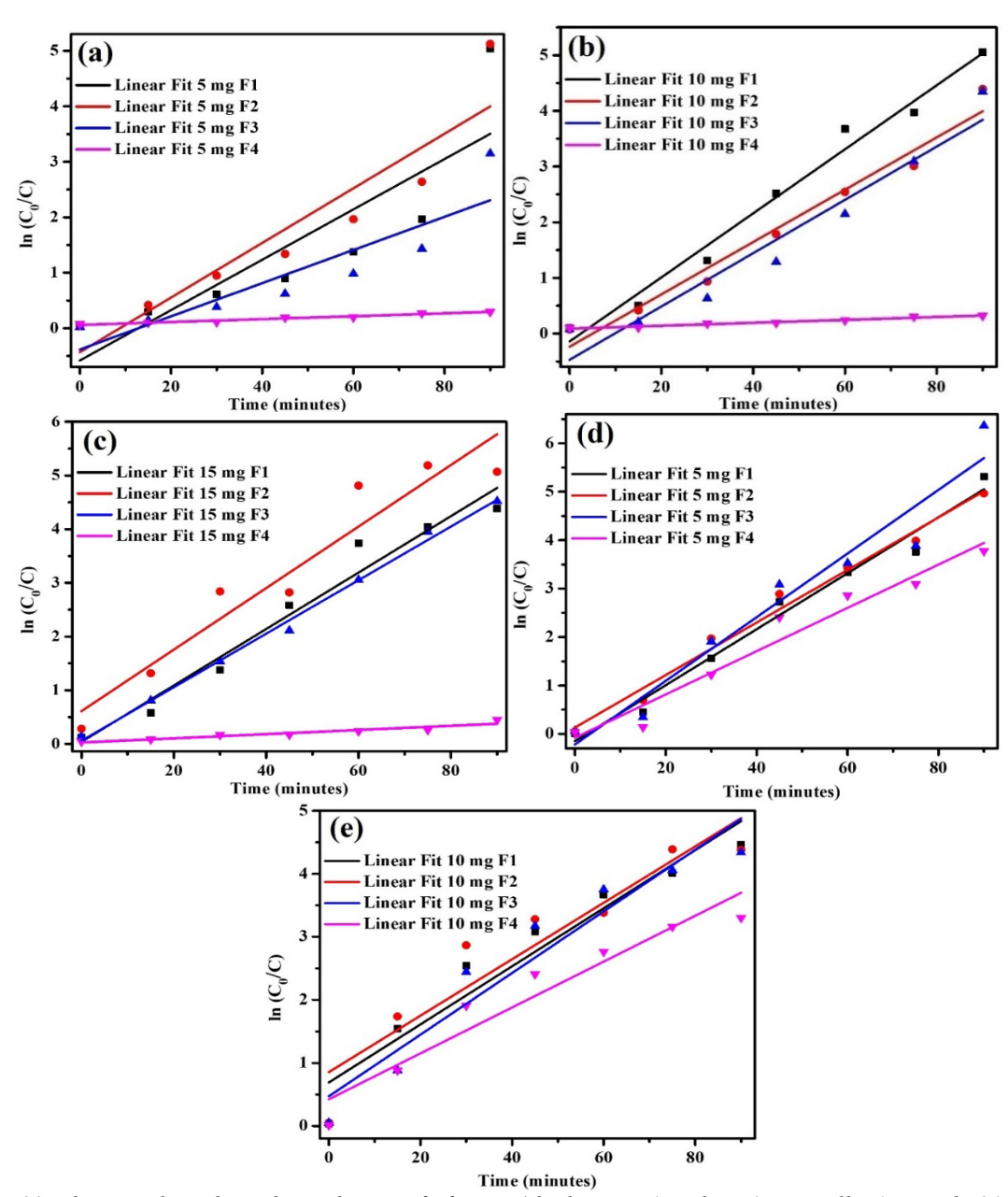


Fig. 11. Photocatalytic degradation kinetics fit for RB (rhodamine B) and EY (eosin yellow). Panels (a), (b), and (c) are linear fit plots for rhodamine B and panels (d) and (e) are linear fit plots for eosin yellow  $[F1 - 60\% TiO_2 - ZrO_2]$ ,  $F2 - 40\% TiO_2 - ZrO_2$ ,  $F3 - pure\ TiO_2$  and  $F4 - pure\ ZrO_2$ .

Photocatalytic degradation of eosin yellow was carried out in the same conditions mentioned above for 5 and 10 mg catalyst concentration. All the samples have shown 96% - 99% degradation at the end of 90 min of visible light irradiation. The samples 60%  $TiO_2 - ZrO_2$ , 40%  $TiO_2 - ZrO_2$  and pure  $TiO_2$  are found to be highly efficient as the dye degraded up to 90% within 60 mins and up to 99% in 90 min of visible light irradiation (Figures 10a, 10b, and 10c). The sample pure  $ZrO_2$  has also shown 96% degradation in 90 min of visible light irradiation, but the rate of degradation appeared to be slower (Figure 10d).

By plotting kinetic graph between  $ln(C_0/C)$  and t (time in min) on y-axis and x-axis respectively rate constant values for dye degradation are calculated and displayed in (Figure 11).

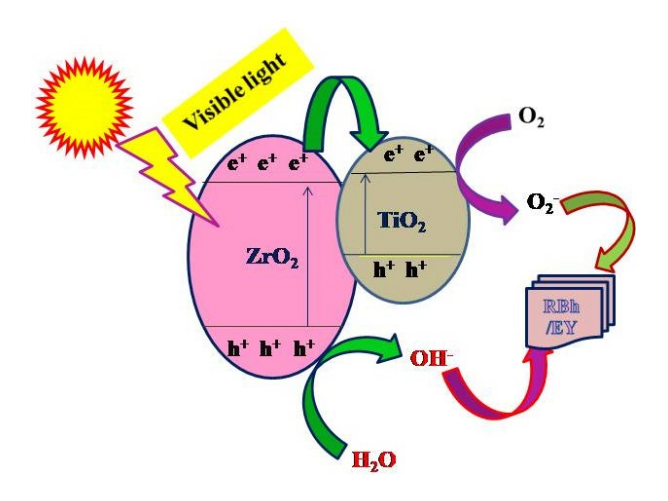


Fig. 12. Photocatalytic Mechanisms of degradation of RB (rhodamine B) and EY (eosin yellow) dyes utilizing a catalyst.

Table 3. Pseudo-first-order kinetics and correlation co-efficient parameters for degradation of RB dye.

Catalyst	Amount of catalyst (mg)	k (min <sup>-1</sup> )	R <sup>2</sup>
	5	0.052579	0.9661
60% TiO2-ZrO2	10	0.057524	0.9133
	15	0.045395	0.7441
	5	0.057619	0.9851
$40\%TiO_2 - ZrO_2$	10	0.047001	0.9721
	15	0.049229	0.8633
	5	0.04989	0.9958
Pure TiO2	10	0.04788	0.9423
	15	0.029906	0.8037
	5	0.003897	0.8960
Pure ZrO <sub>2</sub>	10	0.002625	0.9705
	15	0.002619	0.9623

Catalyst	Amount of catalyst	k (min <sup>-1</sup> )	R <sup>2</sup>
	(mg)		
60% TiO2-ZrO2	5	0.052148	0.9801
	10	0.048891	0.9316
40%TiO2-ZrO2	5	0.057793	0.9861
	10	0.046071	0.8863
Pure TiO2	5	0.054244	0.9465
	10	0.044763	0.9264
Pure ZrO2	5	0.04469	0.9568
	10	0.036397	0.9292

Table 4. Pseudo-first-order kinetics and correlation co-efficient parameters for degradation of EY dye.

The calculated kinetics parameters for RB and EY dye are summarized in the table (3) and table (4). It is inferred that among all the 4 composites F2 shows the higher degradation rate constant for both the dyes with minimal dosage (5 mg) of catalyst.

Because of improved and quicker adsorption kinetics on all catalysts, the rate of photocatalytic degradation of eosin yellow is higher than that of rhodamine B with all samples [39]. The bandgap values of 60% TiO<sub>2</sub>– ZrO<sub>2</sub>, 40%TiO<sub>2</sub>– ZrO<sub>2</sub>, Pure TiO<sub>2</sub> are 3.32 eV, 3.33 eV and 3.34 eV respectively, whereas that of Pure ZrO<sub>2</sub> is 3.69 eV, much higher than the other three samples. These results can be justified as the energy and time required for F4 to degrade the dyes are more than 60%TiO<sub>2</sub>– ZrO<sub>2</sub>, 40%TiO<sub>2</sub>– ZrO<sub>2</sub>. Pure TiO<sub>2</sub>.

Nano TiO<sub>2</sub> is proven to be an efficient photocatalyst due to its reduced electron-hole pair recombination in the electronic bands and a fluctuating bandgap, meanwhile ZrO<sub>2</sub> also has a variable bandgap but it shows comparatively less photocatalytic activity due to the intra-bandgap surface states. This leads to shift in energy states of electrons within conduction band. The composite of TiO<sub>2</sub> and ZrO<sub>2</sub> tuned the bandgap and helped to exhibit significant photocatalytic activities under visible region [40 & 41]. The nanocomposites 60% TiO<sub>2</sub>-ZrO<sub>2</sub> and 40% TiO<sub>2</sub>-ZrO<sub>2</sub> have average particle diameters are 48.1 and 38.63 nm; whereas that of pure TiO<sub>2</sub> and pure ZrO<sub>2</sub> are 71.9 and 66.6 nm, respectively. The nanocomposites have smaller particle sizes when compared to the pure phase of titania and zirconia, and the difference in particle sizes has potentially played a major role in the rate of catalysis. Smaller particles have high surface areas, providing more active sites for catalysis. Particles at nanoscale have high surface area to volume ratio hence their photocatalytic potential increases with the decrease in particle size [42 – 44].

The nanocomposites  $60\% TiO_2 - ZrO_2$  and  $40\% TiO_2 - ZrO_2$  efficiently degraded both rhodamine B and eosin yellow which are cationic dye and anionic dye respectively. Furthermore, it was discovered that the 40% TiO<sub>2</sub>-ZrO<sub>2</sub> catalyst's pseudo-first-order rate constants (5 mg) at a lower dosage were greater than those for the catalyst 60% TiO<sub>2</sub>-ZrO<sub>2</sub> (5 mg). The pseudo-first-order rate constant (k) for dye degradation has increased as the photocatalyst dosage has decreased, as seen in Tables 3 and 4. The rate constant (k) for 40% TiO<sub>2</sub>-ZrO<sub>2</sub> is 0.057619 min<sup>-1</sup> for RB and 0.057793 min<sup>-1</sup> for EY. Both dyes exhibit pseudo-first-order kinetics behaviour in the linear fit between ln (C0/C) and reaction time (t in minutes) (Figure 11) [45–47]. Consequently, the 40% TiO<sub>2</sub>-ZrO<sub>2</sub> catalyst shows a quicker rate constant and increased photocatalytic activity when exposed to visible light.

#### 5. Conclusion

The TiO<sub>2</sub>/ZrO<sub>2</sub> nanocomposite are synthesized via hydrothermal method in two different ratios have been systematically characterized, revealing their well – defined structural, morphological and optical properties. The photocatalytic studies reveals that the influence of 5mg of catalyst dosage has been sufficient to achieve similar degradation efficiencies as higher dosages (10 mg &15 mg). The degradation rate of Eosin Yellow (Anionic dye) has been observed to be higher for 40%TiO<sub>2</sub>/ZrO<sub>2</sub> composite, whereas the 60%TiO<sub>2</sub>/ZrO<sub>2</sub> composition exhibited a higher

degradation rate for Rhodamine B (Cationic dye), attributed to variations in adsorption kinetics and also due to better charge separation, light absorption properties and ROS formation. Consequently, these results demonstrate the  $\text{TiO}_2/\text{ZrO}_2$  nanocomposite's potential as an effective multipurpose material for waste water treatment, antimicrobial coatings and other environmental and biomedical applications.

# Acknowledgements

The author thanks to Sri Sarada college for Women (Autonomous), Salem – 636 016, and Prayoga Institute of Education Research, Bangalore – 560 085, for providing the lab facilities to carry out this research work.

#### References

- [1] Nur Hidayatul Syazwani Suhaimi, Rahil Azhar, Nur Syamimi Adzis, Mohd Azlan Mohd Ishak, Muhammad Zahiruddin Ramli, Mohd Yusof Hamzah, Khudzir Ismail, Wan Izhan Nawawi, Desalina Water Treat 321 (2025) 100976; https://doi.org/10.1016/j.dwt.2024.100976
- [2] Basahel, S. N., Ali, T. T., Mokhtar, M., Narasimharao, K., Nanoscale Res. Lett., 10 (2015) 73; https://doi.org/10.1186/s11671-015-0780-z
- [3] Ren, G., Han, H., Wang, Y., Liu, S., Zhao, J., Meng, X., Li, Z., Nanomaterials, 11 (2021) 1804; https://doi.org/10.3390/nano11071804
- [4] Salvador Cesa, F., Turra, A., Baruque-Ramos, Sci. Total Environ. 598 (2017) 1116-1129; https://doi.org/10.1016/j.scitotenv.2017.04.172
- [5] Vanitha Katheresan, Jibrail Kansedo, Sie Yon Lau, J. Environ. Chem. Eng. 6(2018) 4676-4697; <a href="https://doi.org/10.1016/j.jece.2018.06.060">https://doi.org/10.1016/j.jece.2018.06.060</a>
- [6] C. Karthikeyan, P. Arunachalam, K. Ramachandran, A.M. Al-Mayouf, S. Karuppuchamy, J. Alloys Compd. (2020); <a href="https://doi.org/10.1016/j.jallcom.2020.154281">https://doi.org/10.1016/j.jallcom.2020.154281</a>
- [7] Khan. S., Noor. T., Iqbal. N., Yaqoob. L., ACS Omega, (2024) 21751 21767; <a href="https://doi.org/10.1021/acsomega.4c00887">https://doi.org/10.1021/acsomega.4c00887</a>
- [8] Wu, H., Tan, H. L., Toe, C. Y., Scott, J., Wang, L., Amal, R., Ng, Y. H., Advanced Materials, (2019)1904717; https://doi.org/10.1002/adma.201904717
- [9] Rashid R, Shafiq I, Gilani MRHS, Maaz M, Akhter P, Hussain M, et al., Chemosphere 2023 349; <a href="https://doi.org/10.1016/j.chemosphere.2023.140703">https://doi.org/10.1016/j.chemosphere.2023.140703</a>
- [10] Pareshkumar G. Moradeeya, Archana Sharma, Madhava Anil Kumar, Shaik Basha, Environmental Research, 204 (2022) 112384; https://doi.org/10.1016/j.envres.2021.112384
- [11] Jiang, D., Xu, Y., Wu, D., Sun, Y., J. Solid State Chem. 181 (2008) 593 602; https://doi.org/10.1016/j.jssc.2008.01.004
- [12] Peng, T., Zhao, D., Dai, K., Shi, w., Hirao, K., J. Phys. Chem. B, 109 (2005) 4947 4952; https://doi.org/10.1021/jp044771r
- [13] Rani V, Sharma A, Kumar A, Singh P, Thakur S, Singh A, Le QV, Nguyen VH, Raizada P., Catalysts. 12(11) 2022 1418; <a href="https://doi.org/10.3390/catal12111418">https://doi.org/10.3390/catal12111418</a>
- [14] Renuka L., Anantharaju K.S., Sharma S.C., Nagaswarupa H., Vidya Y.S., Nagabhushana H.P., Prashantha S.C., J. Alloys Compd. 695 (2017) 382-395; <a href="https://doi.org/10.1016/j.jallcom.2016.10.126">https://doi.org/10.1016/j.jallcom.2016.10.126</a>
- [15] Boran, F., Okutan, M., Turk. J. Chem, 47(2) (2023) 448-464; <a href="https://doi.org/10.55730/1300-0527.3551">https://doi.org/10.55730/1300-0527.3551</a>
- [16] Długosz, O., Szostak, K., Banach, M., Appl Nanosci 10, (2020) 941-954; https://doi.org/10.1007/s13204-019-01158-3
- [17] Polisetti, S., Deshpande, P.A., Madaras, G., Ind. Eng. Chem. Res. 50 (2011) 12915 12924; https://doi.org/10.1021/ie200350f

- [18] Kumari P, Saha R, Saikia G, Bhujel A, Choudhury MG, Jagdale P, Paul S., Toxics. 11(3) (2023) 234; <a href="https://doi.org/10.3390/toxics11030234">https://doi.org/10.3390/toxics11030234</a>
- [19] Bansal, Pratibha; Chaudhary, Ganga Ram; Mehta, S.K. . (2015), Chemical Engineering Journal, 280, 475-485; <a href="https://doi.org/10.1016/j.cej.2015.06.039">https://doi.org/10.1016/j.cej.2015.06.039</a>
- [20] Manivannan, Ramalingam; Ryu, Jiwon; Son, Young-A., Colloids and Surfaces A: Physicochemical and Engineering Aspects, 608, 125601; https://doi.org/10.1016/j.colsurfa.2020.125601
- [21] Elsisi, M.E., Mansour, A.F., Sci Rep 15, 19120 (2025);

https://doi.org/10.1038/s41598-025-03306-y

[22] Martins, Pedro; Kappert, Sandro; Nga Le, Hoai; Sebastian, Victor; Kuhn, Klaus; Alves, Madalena; Pereira, Luciana; Cuniberti, Gianaurelio; Melle-Franco, Manuel; Lanceros-Mendez, Senentxu, (2020) Catalysts, 10(2), 234;

https://doi.org/10.3390/catal10020234

- [23] N.N. Bahrudin, Applied Surface Science Advances, 7, 2022, 100208; https://doi.org/10.1016/j.apsadv.2021.100208
- [24] Vaizoğullar, Ali İmran & BALCI, Ahmet & Uğurlu, Mehmet, Hamdi, Mohammad, AKU J. Sci. Eng. 16(2016) 54-60; <a href="https://doi.org/10.5578/fmbd.25229">https://doi.org/10.5578/fmbd.25229</a>
- [25] Priyanka Basyach, Madhabi Devi, Amarjyoti Choudhury, Journal of Material science and Mechanical Engineering, 3 (2016) 511 514, Krishi Sanskriti Publications.
- [26] Masoud Habibi Zare, Arjomand Mehrabani Zienabad, Sci. Rep., 12 (2022) 10388; <a href="https://doi.org/10.1038/s41598-022-14676-y">https://doi.org/10.1038/s41598-022-14676-y</a>
- [27] Asha R Pai, Bipin Nair, Bull. Mater. Sci., 38 (2015) 1129 1133; https://doi.org/10.1007/s12034-015-0991-z
- [28] Yaacob, N., Ismail, A.F., Sean, G.P. et al., SN Appl. Sci. 1, 252 (2019); https://doi.org/10.1007/s42452-019-0247-4
- [29] Nhlengethwa, S.T.; Tshangana, C.S.; Mamba, B.B.; Muleja, A.A. Membr, 14 (2024) 222; https://doi.org/10.3390/membranes14100222
- [30] T.V.L. Thejaswini, D. Prabhakaran, M. Akhila Maheswari, J. Photochem. Photobiol. A Chem., 344 (2017) 212-222; <a href="https://doi.org/10.1016/j.jphotochem.2017.05.015">https://doi.org/10.1016/j.jphotochem.2017.05.015</a>
- [31] Anwer, H., Mahmood, A., Lee, J. et al., Nano Res. 12 (2019) 955-972; https://doi.org/10.1007/s12274-019-2287-0
- [32] Ruíz-Santoyo, V. Marañon-Ruiz, V.F. Romero-Toledo, R. González Vargas, O.A. Pérez-Larios, A., Catal., 11 (2021) 1035; <a href="https://doi.org/10.3390/catal11091035">https://doi.org/10.3390/catal11091035</a>
- [33] N. Venkatachalam, M. Palanichamy, Banumathi Arabindoo, V. Murugesan, J. Mol. Catal. A: Chem., 266 (2007) 158-165; https://doi.org/10.1016/j.molcata.2006.10.051
- [34] Revathi, V., Karthik, K., J Mater Sci: Mater Electron 29 (2018) 18519-18530; <a href="https://doi.org/10.1007/s10854-018-9968-1">https://doi.org/10.1007/s10854-018-9968-1</a>
- [35] Keskin C.S., Ozdemir A., Karabayir E., Sengil I.A., Environ. Prot. Eng., 39 (2013) 119 133; <a href="https://doi.org/10.37190/epe130309">https://doi.org/10.37190/epe130309</a>
- [36] Shimi, Annin Ahmed, Hiwa Wahab, Muhammad Katheria, Snehlata Wabaidur, Saikh Eldesoky, Gaber Rane, Kantilal, J. Nanomater. (2022); https://doi.org/10.1155/2022/7060388
- [37] Swagata Banerjee, Suresh C. Pillai, Polycarpos Falaras, Kevin E. O'Shea, John A. Byrne, Dionysios D. Dionysiou, J. Phys. Chem. Lett. 2014, 5, 15, 2543-2554; https://doi.org/10.1021/jz501030x
- [38] Qingzhe Zhang, Deepak Thrithamarassery Gangadharan, Yanlong Liu, Zhenhe Xu, Mohamed Chaker, Dongling Ma, Journal of Materiomics, 3 (1), 2017, 33-50; https://doi.org/10.1016/j.jmat.2016.11.005
- [39] Gobouri, A.A., Res Chem Intermed 42, 5099-5113 (2016); https://doi.org/10.1007/s11164-015-2347-0

- [40] M.A. Rauf, S. Salman Ashraf, Chemical Engineering Journal, Volume 151 (1-3), 2009, 10-18; https://doi.org/10.1016/j.cej.2009.02.026
- [41] C. de M. da Trindade, S.W. da Silva, J.P. Bortolozzi, E.D. Banús, A.M. Bernardes, M.A. Ulla, Applied Surface Science, 457, 2018, 644-654; <a href="https://doi.org/10.1016/j.apsusc.2018.06.287">https://doi.org/10.1016/j.apsusc.2018.06.287</a>
- [42] Mamotaj Khatun, Partha Mitra, Sanjoy Mukherjee, Hybrid Advances, 4, (2023), 100079; https://doi.org/10.1016/j.hybadv.2023.100079
- [43] Muthuvel, A., Jothibas, M., Manoharan, C., Nanotechnol. Environ. Eng. 5, 14 (2020); https://doi.org/10.1007/s41204-020-00078-w
- [44] Buledi, J.A., Pato, A.H., Kanhar, A.H. et al., Appl Nanosci 11, 1241-1256 (2021); https://doi.org/10.1007/s13204-021-01685-y
- [45] Hyun Jung Lee, Joo Hyun Kim, Seong Soo Park, Seong Soo Hong, Gun Dae Lee, Journal of Industrial and Engineering Chemistry, 25, (2015), 199-206; https://doi.org/10.1016/j.jiec.2014.10.035
- [46] Lan, Shi, Liu, Lu, Li, Ruiqing, Leng, Zhihua, Gan, Shucai, Ind. Eng. Chem. Res. (2014), 53, 8, 3131-3139; <a href="https://doi.org/10.1021/ie404053m">https://doi.org/10.1021/ie404053m</a>
- [47] Buledi, Jamil Pato, Abdul Hyder, Ali Solangi, Amber Batool, Madeeha Ameen, Sidra Palabiyik, Ismail, Appl. Nanosci. 11 (2021) 1241-1256; <a href="https://doi.org/10.1007/s13204-021-01685-y">https://doi.org/10.1007/s13204-021-01685-y</a>